

Greenhouse Gases Observing Satellite -2
(GOSAT-2)
Level-1 Algorithm Theoretical Basis Document
for TANSO-FTS-2
v200

Rev. NC Oct. 2020

Japan Aerospace Exploration Agency

Rev.	Date	Revision Contents	Remark
NC	Oct. 30. 2020	-	-

Table of contents

1. Introduction.....	4
1.1 Objectives and Scope of this Document	4
1.2 Applicable Documents (all in Japanese).....	4
1.2.1 Applicable documents	4
1.2.2 Reference documents.....	4
1.3 Overview of TANSO-2 (Hardware).....	5
1.3.1 GOSAT-2 satellite	5
1.3.2 Greenhouse gases observing sensor: TANSO-FTS-2.....	5
2. Observation Requirements, Plan and Data Processing.....	8
2.1 Observation Requirements and Plan	8
2.1.1 Nominal operation.....	8
2.1.2 Observation plan	8
2.1.3 Calibration requirements	9
2.2 TANSO Data Overview.....	9
2.2.1 Concept of data flow	9
2.3 Level-1 Processing for TANSO-FTS-2.....	11
2.3.1 Brief description of Level-1 processing for FTS-2	11
2.3.2 Processing for uniform time sampling to OPD sample	12
2.3.3 Processing for band1-3 spectra	16
2.3.4 Processing for Band 4-5 spectra	22
2.3.5 Quality control	35
2.3.6 Observation time.....	37
2.3.7 Processing for line of scene	37
2.4 TANSO-FTS-2 Acronyms.....	38
2.5 TANSO-FTS-2 reference	39

1. Introduction

1.1 Objectives and Scope of this Document

This technical document describes an overview of the data processing methodologies of science sensors, Level 1 (hereafter L1) algorithms to be used for ground-based data processing, observation and calibration requirements of the L1 algorithms, and the hardware of science sensors onboard the Greenhouse gasses Observing SATellite-2 (hereafter GOSAT-2) developed by the Japan Aerospace Exploration Agency (JAXA). The science sensors onboard the GOSAT-2 satellite include the Thermal And Near infrared Sensor for carbon Observation – Fourier Transform Spectrometer-2 (hereafter TANSO-FTS-2 or simply FTS-2) and the Cloud and Aerosol Imager-2 (TANSO-CAI-2 or simply CAI-2).

This document should be used as a baseline for the development of a design specifications document on the L1 data processing algorithms for TANSO-FTS-2.

1.2 Applicable Documents (all in Japanese)

1.2.1 Applicable documents

none

1.2.2 Reference documents

none

1.3 Overview of TANSO-2 (Hardware)

1.3.1 GOSAT-2 satellite

GOSAT-2 monitors carbon dioxide (CO₂) and methane (CH₄) globally from space. GOSAT-2 is placed in sun-synchronous orbit (613 km) at 13:00 local time, with an inclination angle of 98° . The revisit time of GOSAT-2 is six days. Fig. 1.3.1-1 shows an on-orbit image of GOSAT-2.



Fig. 1.3.1-1. Satellite image of GOSAT-2 and its two instruments

Table 1.3.1-1 lists the specification of the GOSAT-2 orbit trajectory.

Table 1.3.1-1. Orbit conditions for GOSAT-2

	Specification Items	Specifications	Remarks
O R B I T	Type	Sun synchronous, quasi-recurrent	
	Local sun-time for the Descending node	13 hours ± 15 minutes	
	Altitude	612.98 km	(Not including altitude variations in an orbit)
	Inclination	97.84 degrees	
	Eccentricity	0.00106	(Frozen orbit)
	Period	Approximately 98.1 minutes	
	Orbit repeat	6 days (89 paths)	
	Descending node longitude	fly over Lamont (latitude 36.6 north, longitude 97.5 west)	
Descending node accuracy	± 2.5 km	(Depending upon the frequency of orbit control maneuvers)	

1.3.2 Greenhouse gases observing sensor: TANSO-FTS-2

The greenhouse gases observing sensor measures the spectra of short-wave infrared light that passes through Earth's atmosphere and is reflected by Earth's surface, and thermal infrared light in Earth's

atmosphere. First, the gaseous column amounts (column abundance) of CO₂ and CH₄ in the 1.6 μm band, CO₂ in the 2.0 μm band, and CH₄ and CO in the 2.3 μm band are estimated. Then the gaseous concentration profile (vertical distribution) is assessed utilizing the thermal infrared wavelength region. A Fourier interferometer that enables observation with high spectral resolution (0.2 cm⁻¹) for a wide bandwidth of wavelengths should be used. An interferogram created in 4.024 seconds is set as a baseline. A two-axis pointing control mechanism should be utilized, while allowing the sensor to be pointed at the same observation location (grid footprint) for one interferogram, so as to scan the cross-track direction and complete a sun glint observation. A Fourier interferometer is applied with a double cube corner type, and a long-life diode laser light source of 1.31 μm is adopted to meet the long-life mission requirement of five years. Three types of detectors are used: one made of Si, one made of PV-MCT to facilitate a passive cooler for detector cooling, and one made of PC-MCT that also facilitates a passive cooler for detector cooling. A polarized beam splitter in the observation sensor optics enables simultaneous observation of two linear polarizations for 0.76 μm, 1.6 μm, and 2.0–2.3 μm.

Solar irradiance calibration is performed using a short-wave infrared diffuser, followed by on-orbit thermal infrared radiometric calibration using a blackbody. Lunar calibration is conducted about once a month. Instrumental Line Shape (ILS) function calibration is also performed using two types of diode lasers: 0.76 μm and 1.55 μm.

Fig. 1.3.2-1 shows an overview of the TANSO-FTS-2 system, and Fig. 1.3.2-2 shows a mounting image on the satellite deck.

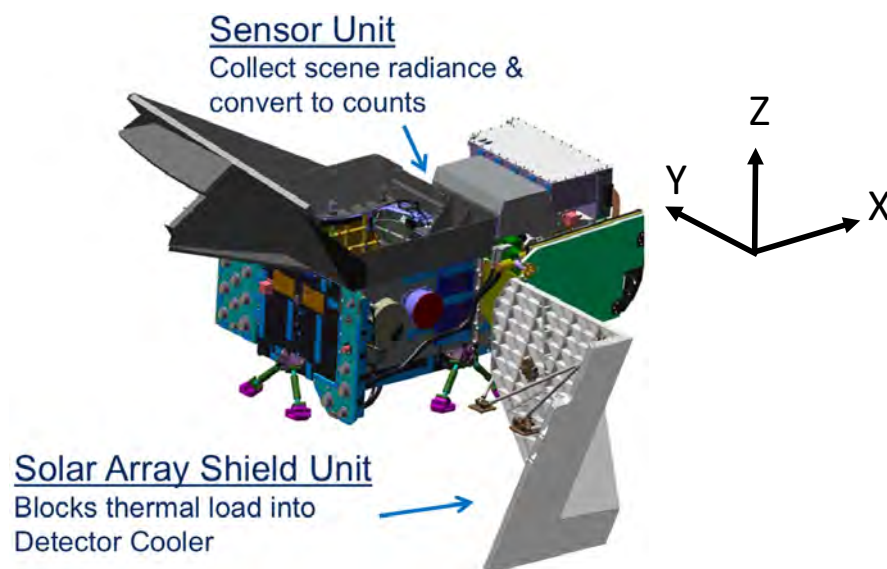


Fig. 1.3.2-1. Overview of TANSO-FTS-2

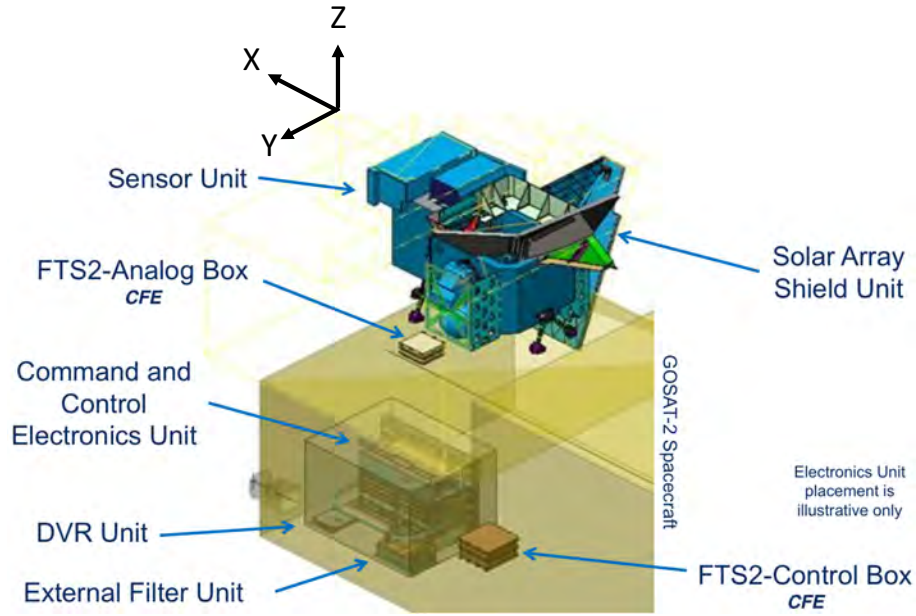


Fig. 1.3.2-2. Mounting image on the satellite deck

Table 1.3.2-1. Main characteristics of TANSO-FTS-2

	Band1	Band2	Band3	Band4	Band5
Polarization Obs.	Yes	Yes	Yes	No	No
Ranges (cm ⁻¹)	12950-13250	5900-6400	4200-5200	1188-1800	700-1188
Sampling Interval (cm ⁻¹)	0.2 cm ⁻¹ (Double-sides scan) (MOPD +/-2.5 cm)				
Sampling Num.	153090	76545	76545	38250	38250
Resolution (cm ⁻¹)	< 0.4	< 0.27	< 0.27	< 0.27	< 0.27

2. Observation Requirements, Plan and Data Processing

2.1 Observation Requirements and Plan

2.1.1 Nominal operation

Normal scanning observation (i.e., fixed grid observation points) and sampling observation (i.e., medium to low latitude observation points over oceans where sun glint observations are to be conducted) should be done according to a certain set pattern and should be determined before the events.

The particular time of a sun-illuminated period of the satellite flight (e.g., for a solar irradiance calibration) and the particular daytime on Earth's surface (e.g., for starting normal observation) should be specified by ground commands as a function of a geo-location.

The observations at a set point for a validation purpose as well as for monitoring megacity emissions should be planned ahead of the events. Fig. 2.1.1-1 shows a schematic diagram of TANSO-2 operation.

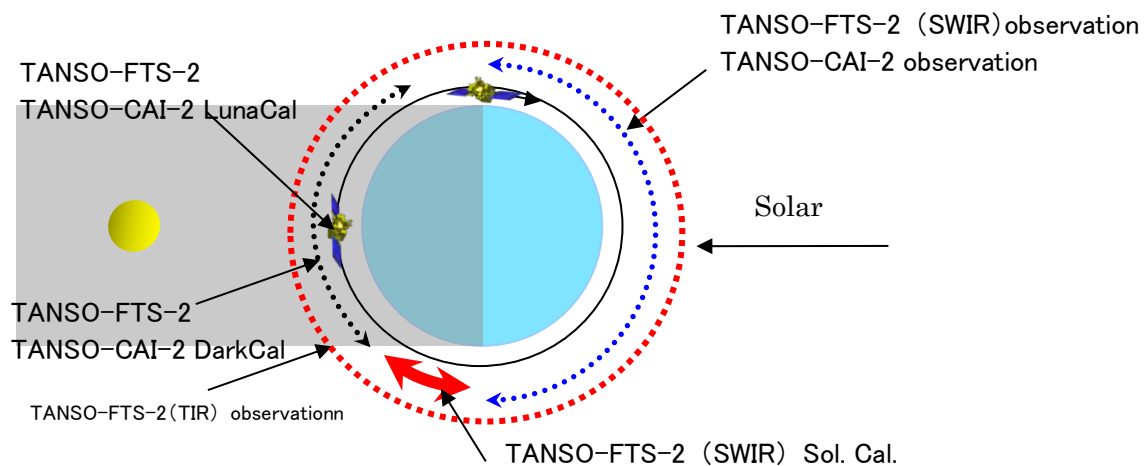


Fig. 2.1.1-1. Overview of TANSO-2 operation

2.1.2 Observation plan

The albedo of Earth's surface is estimated from the observation data of the GOSAT-2 satellite, and estimation accuracy will be enhanced when the same footprint location is observed every six days. For this reason, (within the sensor) TANSO-FTS-2 conducts FTS-modulator scan period tuning after receiving the GOSAT-2 satellite's orbital information including the GPS signal. A particular orbital trajectory that facilitates an exact flyover of Lamont (latitude 36.60 north, and longitude 97.49 west) should be selected for this purpose. An observation interval is 4.024 seconds, and the turnaround time is 0.65 seconds for one observation. The observation locations are calculated in the Mission operation Management Organization (MMO) system. A maximum number of 1246 observation points are set per orbit, with an equal time difference. For scanner motor safety, the difference in optical angle between two observation angles must be kept at a 25.5 degrees in line with the scene angle. If the motor receives an angle command that exceeds the limit, TANSO-FTS-2 immediately transits from operation mode to diagnostic mode.

2.1.3 Calibration requirements

In one orbit, TANSO-FTS-2 conducts sun irradiance calibration, deep space calibration and blackbody calibration, all with a set pattern. Conducting deep space pattern calibration and blackbody pattern calibration at a fixed timing will adversely affect observations of certain latitudes. For this reason, calibration operations that facilitate uniform data acquisition should be considered.

Electrical calibration is conducted at night once in about one month, and must be examined to satisfy the thermal design requirements of the sensor.

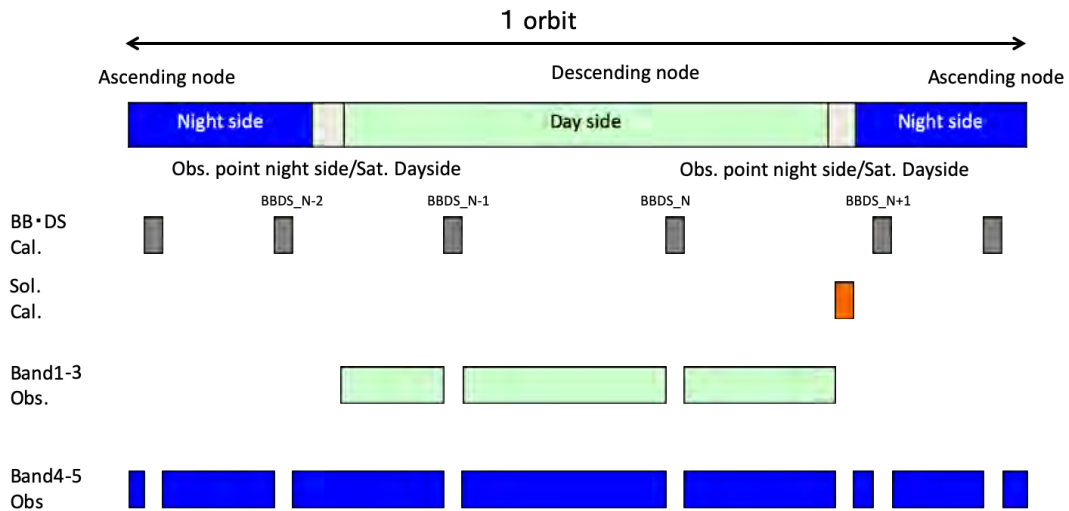


Fig. 2.1.3-1. Typical calibration operation in one-orbit

2.2 TANSO Data Overview

2.2.1 Concept of data flow

Table 2.2.1-1 illustrate the basic concept of data flow.

Table 2.2.1-1. Concept of TANSO data flow

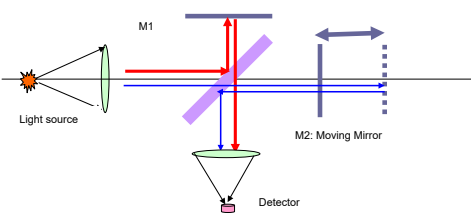
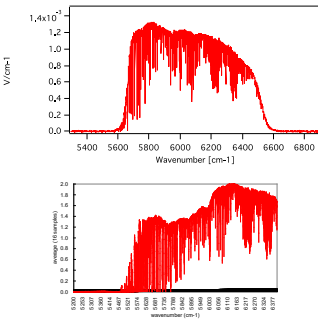
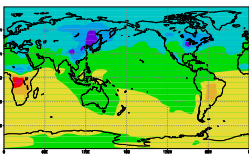
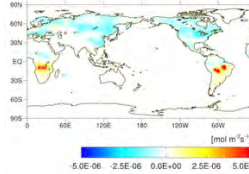
Processing/Products	Concept diagram	Supplementary explanation
Photoelectric conversion of observation light		<p>Observation light is modulated by Fourier interferometer, performed photoelectric conversion (photon to current) at detector, and converted to voltage by the first stage amplifier.</p>
Equal-timing interferogram L1A/UTS		<p>Record voltage at the time synchronized to internal clock by each band. Therefore, the horizontal-axis shows time and the vertical-axis shows voltage. Record the zero point passage time simultaneously. These data are transmitted to the ground system.</p>
Equal-distance interferogram L1A		<p>Convert equal-timing interferogram into equal-distance interferogram. In this result, horizontal-axis shows optical path difference and the vertical-axis shows voltage.</p>
Spectrum L1B		<p>(FTS-2 SWIR) Observation spectrums before sensitivity calibration (V/cm^{-1}) and after sensitivity calibration ($W/cm^2/str/cm^{-1}$)</p> <p>(FTS-2 TIR) Spectrum after sensitivity calibration using blackbody/deep space calibration data ($W/cm^2/str/cm^{-1}$) and spectrum adopted effective FOV correction ($W/cm^2/str/cm^{-1}$)</p>
Column amount concentration L2	<p>(SWIR) XCO₂ = 400.0 ppm (ex.) XCH₄ = 1.90 ppm (ex.)</p> <p>(TIR) CO₂@500hPa = 400.0 ppm (ex.) CH₄@500hPa = 1.95 ppm (ex.)</p>	<p>(SWIR) Column-averaged dry-air mole fraction derived from observation spectrum</p> <p>(TIR) Vertical profiles of gas concentrations derived from observation spectrum</p>
Global distribution of column amount concentration L3 (TBD)		<p>Global distributions of CO₂ and CH₄ concentrations</p>
Global flux L4A		<p>Net emissions and uptake of CO₂ and CH₄</p>

Fig. 2.2.1-1 shows the data flow between L0 and L1B.

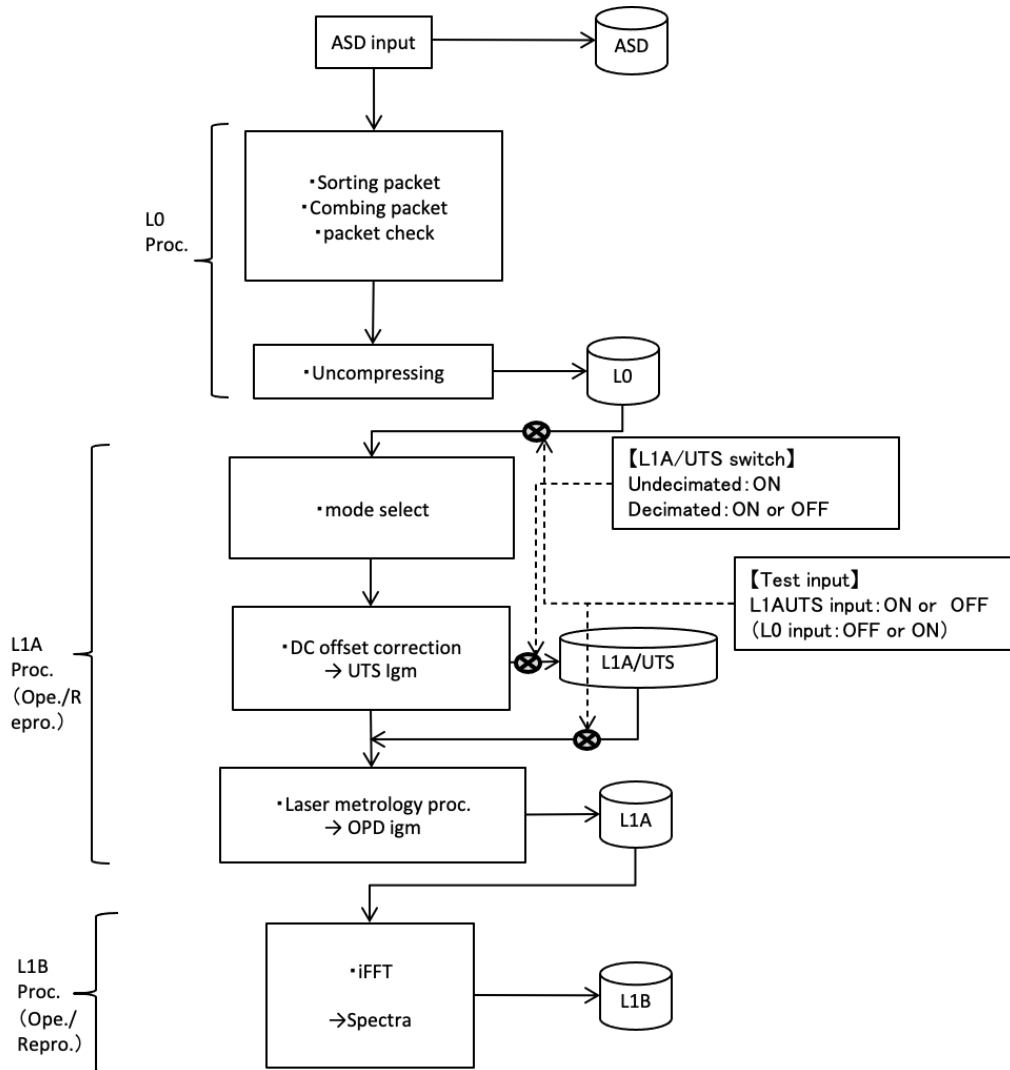


Fig. 2.2.1-1. Data flow (L0 to L1B)

2.3 Level-1 Processing for TANSO-FTS-2

2.3.1 Brief description of Level-1 processing for FTS-2

Level-1 processing for FTS-2 is composed of the three modules listed below.

- Transform from uniform time-sampled interferogram to optical path difference interferogram
- Transform from SWIR interferogram to SWIR spectra (Bands 1,2 and 3)
- Transform from TIR interferogram to TIR spectra (Bands 4 and 5)

The uniform time-sampled interferogram is compressed in orbit and transmitted to the ground. The compressed interferogram is retrieved on the ground.

2.3.2 Processing for uniform time sampling to OPD sample

Both the interferogram and metrology laser zero-crossing periods are recorded at the originated master clock timing. The time-based interferogram and pulse-counter value between zero-crossing periods are transmitted to the ground. The start of observation is synchronized with the sampling window signal provided by the interferometer module. In the processing, the uniform time-sampled interferogram is transformed to the OPD sampled interferogram.

STEP_TO1: Uniform time-sampled interferogram and saturated signal detection

The uniform time-sampled interferogram is constructed with DC offset and gain correction. The equation for uniform time sampled interferogram is described in Eq. 2.3.2-1 describes the uniform time-sampled interferogram

$$I_{amp,b,d}^X = \frac{ADC_scale_b}{PGA_{gain_b}^X} \cdot DN_{b,d}^X \cdot +DAC_{scale_b} \cdot DC_{offset_{b,d}}^X + V_{offset,b}$$

Eq. 2.3.2-1

where,

b : Bands (bands 1P, 1S, 2P, 2S, 3P, 3S, 4, 5)

d : Scan direction (Forward=1, Backward=0)

X : Observation target (nadir obs., Black body Cal., Deep Space Cal., Solar Cal., Luna Cal., ILS Cal., Dark Cal.)

$I_{amp,b,d}^X$: Uniform time-sampled interferogram applied DC offset and gain correction

ADC_scale_b : ADC conversion scale

$DN_{b,d}^X$: Digital number for each interferogram just after the uncompressing

$PGA_{gain_b}^X$: Gain factor for each band

DAC_scale_b : Digital to analog conversion factor for each band

$DC_{offset_{b,d}}^X$: DC offset clamped at observation start period

If the interferogram value at ZPD is equal to or greater than the full bits for each band, a quality warning flag is set for each band. Saturated data are generally not suitable for data processing. As the saturation situation is identifiable by means of a quality (warning) flag, however the data will be applied to inverse Fourier transform and stored as part of the L1B data.

STEP_TO2: Spike signal detection and its correction

Spikes may enter affected by the effects of radiation, particularly when a satellite flies over the South Atlantic Ocean.

If a spike is included in the interferogram, the quality (warning) flag is stored in a file. The effects of radiation are generally represented in an interferogram as a discontinuity signal. Then, the spike signal might be able to distinguish the continuous components. Eq. 2.3.2-2 and Eq. 2.3.2-3 are the equations for identifying the spike signal. The entire interferogram is separated in blocks with N_{spike} points, and then the maximum and minimum values are processed without an offset. If the amplitude for each window exceeds the criteria, the

warning flags are applied.

Fig. 2.3.2-1 shows a schematic diagram for spike detection.

$$\frac{\text{abs}\left(\max\left(DN_{b,d}^x(n:n+N_{spike})\right)\right)}{\text{abs}\left(\min\left(DN_{b,d}^x(n:n+N_{spike})\right)\right)} > spike_{b,max}$$

Eq. 2.3.2-2

$$\frac{\text{abs}\left(\min\left(DN_{b,d}^x(n:n+N_{spike})\right)\right)}{\text{abs}\left(\max\left(DN_{b,d}^x(n:n+N_{spike})\right)\right)} > spike_{b,min}$$

Eq. 2.3.2-3

where, $n = 1:N_{spike}$: Sample size

Theoretically, a one-point spike signal creates high-frequency noise widely in the frequency domain, after inverse Fourier transform. To reduce this undesirable noise, a spike signal correction technique is applied. In case of a spike, the N th sampled data is replaced as the averaged values of the $N - 1$ th and $N + 1$ th samples. In case of the edge of interferogram, the $N = 2$ or $N = end - 1$ sample will be applied.

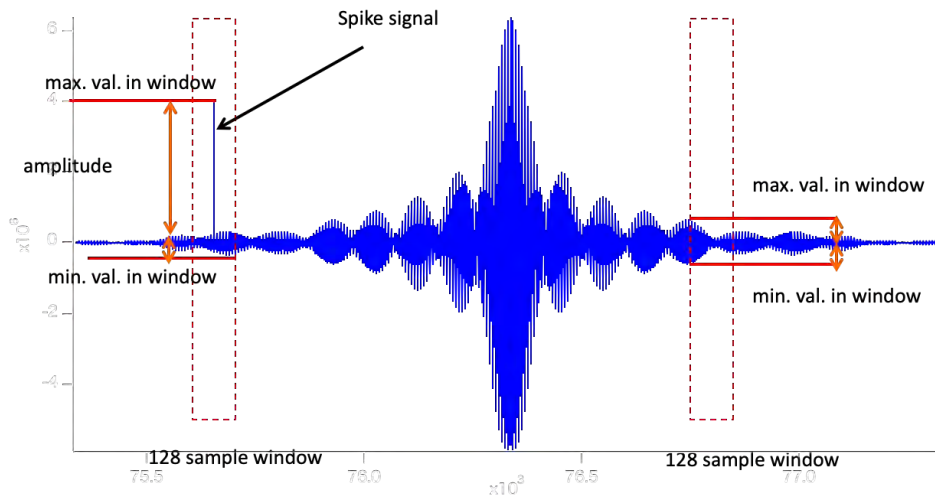


Fig. 2.3.2-1. Schematic diagram for spike detection

STEP_TO3: Processing for time tag data

Fig. 2.3.2-2 shows the timing chart between the metrology laser signal and the sampled interferogram. The sampling window signal is synchronized with scan motion of the interferometer.

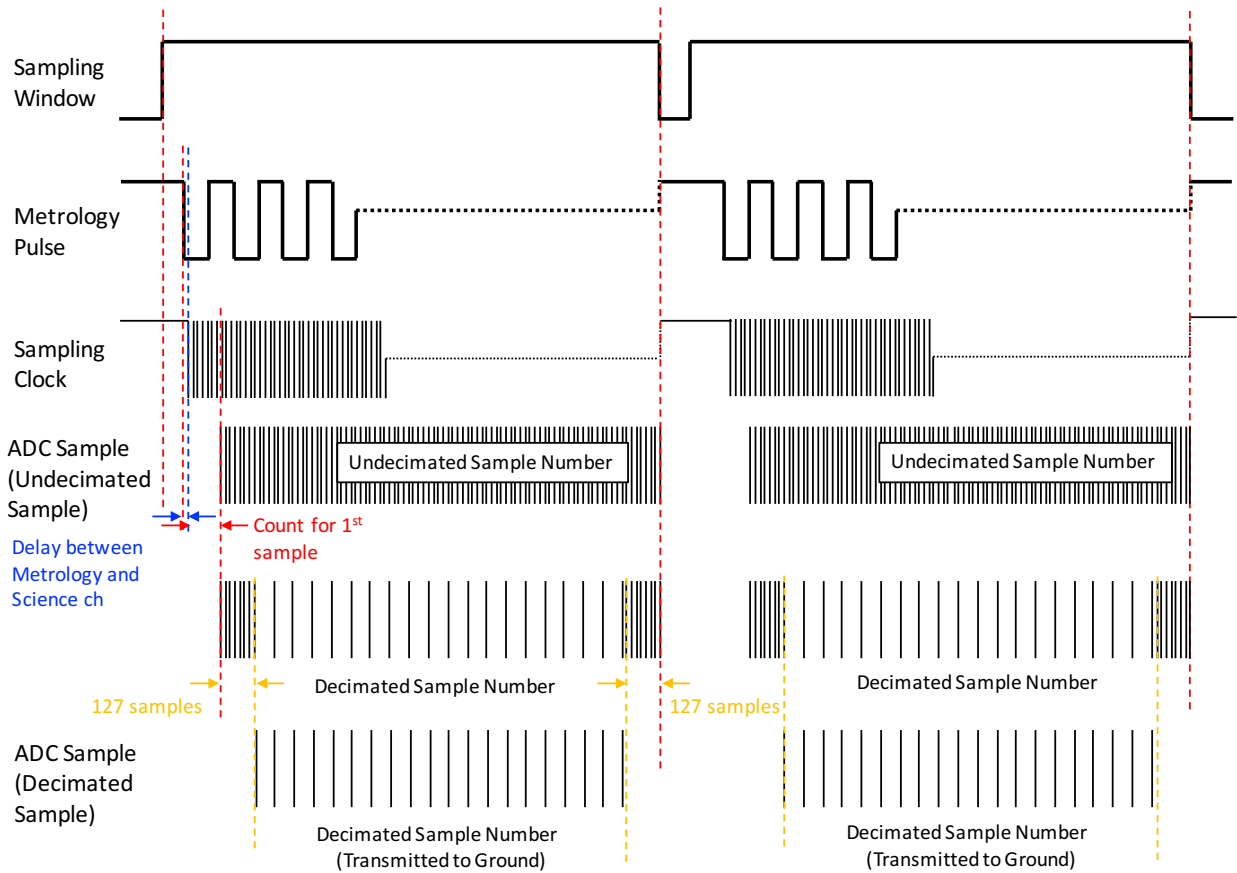


Fig. 2.3.2-2. Timing chart between metrology laser signal and sampled interferogram

When the metrology pulse is active, the sampling clock is counted as an indicator of the sampling interval time. Then the counted value is transmitted as the interval of the metrology pulse. The nominal value is 3458 counts. In parallel, the nominal sampling frequency is 117kHz.

The observed interferometric signal is converted from analog to digital with ADC, which is triggered by a master clock (Sampling Clock). The sampling interval for the original observation signal is 8.547μs. Then, the original sample is called an Undecimated Sample.

Generally, the delay between the metrology pulse and science signal is not zero. In the processing, these time delays must be considered.

In the nominal observation mode, the signal is decimated with specific values. Therefore, the decimated science signal is transmitted to the ground, and retrieved to atmospheric spectra. In parallel, the metrology time data are also transmitted as counts to the ground. The sampling number of the metrology signal is a fixed value of 76789. Eq. 2.3.2-4 expresses the time interval between metrology fringes (zero-crossing points).

$$T_{met_t}[n] = \sum_{k=1}^n T^{met_raw}[k] \cdot \frac{1}{Clock_{master}}, n = 1 \dots N$$

Eq. 2.3.2-4

To make up sampling (for band 1) and down sampling (for bands 4 and 5), the observed fringe interval

will be interpolated by applying Eq. 2.3.2-5.

$$\begin{aligned}
 T_{met}^b[n] &= interp1(1:N, T_{met_t}[N], 1:2N) \quad n = 1, \dots (2 * N), \text{ for } b = \text{Band 1} \\
 T_{met}^b[n] &= T_{met_t}[n], \quad n = 1, \dots N, \text{ for } b = \text{Band 2, 3} \\
 T_{met}^b[n] &= T_{met_t}[2n - 1], \quad n = 1, 2, 3, \dots \left(\frac{N}{2}\right), \text{ for } b = \text{Band 4, 5}
 \end{aligned}$$

Eq. 2.3.2-5

STEP_T05: Processing for OPD sampled interferogram

To process the OPD sampled science interferogram, time sampled science interferogram is coupled with the time-sampled metrology signal, because the metrology signal has both the time and OPD domains.

Sampled time for science signal in time domain is expressed as Eq. 2.3.2-6 expresses sampled time for the science signal in the time domain. In this case, Table 2.3.2-1 lists the sampling parameters.

Table 2.3.2-1, Sampling frequency and sampling parameters

Band	Sampling frequency	Decimation	Effective sampling frequency	Effective sampling interval
B1P/S	234.5kHz	5	46.8kHz	2.1326E-05 sec
B2P/S	117.2kHz	5	23.4kHz	4.2651E-05 sec
B3P/S	117.2kHz	6	19.5kHz	5.1282E-05 sec
B4	117.2kHz	12	9.77kHz	10.2364E-05 sec
B5	117.2kHz	12	9.77kHz	10.2364E-05 sec

$$t_b = T_{met}^b \left[\text{floor} \left(\frac{\text{numBand}_b - \text{numF}}{2} \right) - nZPD_b; \text{floor} \left(\frac{\text{numBand}_b - \text{numF}}{2} \right) - nZPD_b + \text{numBand}_b \right]$$

Eq. 2.3.2-6

where,

numBand_b : Effective sampling number for each band

numF : Sampling points for metrology count

Eq. 2.3.2-7 expresses the sampled time for time-sampled science interferogram (n_b)

$$\begin{aligned}
 T_{b,s} &= \frac{\text{SamplingPulseAdjustment} + 448}{\text{UpsamplingFactor}} \\
 n_b &= \text{floor} \left(\frac{t_i - T_{b,0} - 127 \cdot T_{b,s} - \text{Delay}_{b,side}}{T_{b,s} \cdot \text{DecimationFactor}} \right)
 \end{aligned}$$

Eq. 2.3.2-7

The phase between each sample point is as follows;

$$\Delta t = t_i - T_{b,0} - 127 \cdot T_{b,s} - \text{Delay}_{b,side} - T_{b,s} \cdot n \cdot \text{DecimationFactor}$$

$$P_i = \text{floor} \left(\frac{\Delta t}{T_{b,s} \cdot \text{DecimationFactor}} \cdot P_b \right)$$

Eq. 2.3.2-8

where P_b : Amplitude of digital filter for each bands

Finally, OPD sampled interferograms are processed from Eq. 2.3.2-9 below.

$$I_{opd,b,d}^x = \sum_{k=0}^{M_b-1} I_{amp,b,d,n+\frac{M_b}{2}-k}^x \cdot \text{tap}_{b,p_i,k}$$

Eq. 2.3.2-9

STEP_TO6: Nonlinear correction

The PV-MCT detector is used for bands 2-4, and PC-MCT is used for band 5. MCT is generally characterized by a nonlinear response. If the response cannot be negligible, the higher term of the interferogram must be taken into consideration.

Theoretically, when an artificial signal arises up in the out-of-band region, its detector has a nonlinear response. Thus, the nonlinear correction terms are characterized by checking out-of-band signal intensity.

Eq. 2.3.2-10 expresses a nonlinear corrected OPD sampled iterferogram.

$$I_{nlc,b,d}^x = I_{opd,b,d}^x + a_{nlc,b} \cdot I_{opd,b,d}^x{}^2 + b_{nlc,b} \cdot I_{opd,b,d}^x{}^3 + c_{nlc,b}$$

Eq. 2.3.2-10

where,

$a_{nlc,b}, b_{nlc,b}, c_{nlc,b}$: Nonlinear correction terms for 2nd and 3rd orders, and offset for each band

2.3.3 Processing for band1-3 spectra

This subsection describes an overview of the OPD sampled interferogram (called simply an interferogram) transform to spectra.

Fig. 2.3.3-1 shows a schematic diagram of the processing flow for SWIR bands.

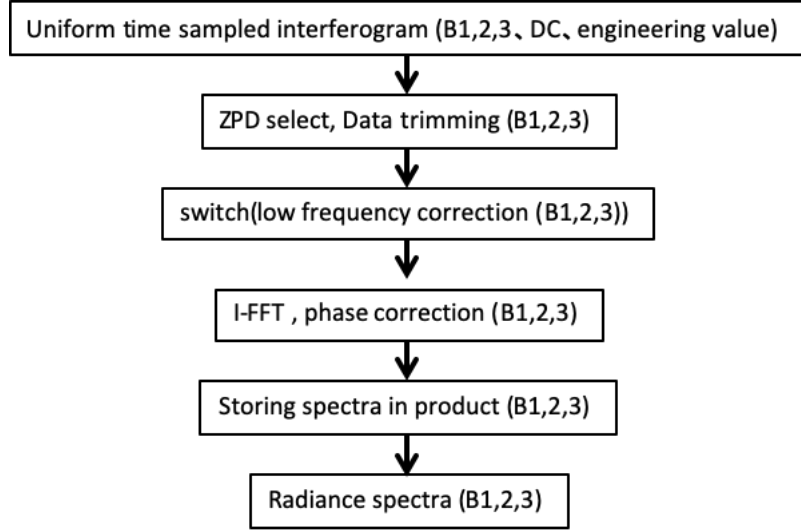


Fig. 2.3.3-1. Processing flow for SWIR bands

STEP_S1: Data trimming

Optical and mechanical ZPD positions are generally not equal. To identify the optical ZPD position, the ZPD position is processed as follows: First, the maximum signal points around the sampling center are detected. Second, fringe count error (FCE) is calculated and applied for correction of the ZPD position. FCE is processed with a truncated interferogram around the maximum signal position ($I_{nlc,b,d}^X$) with truncation size ($FCE_{b,window}$). Then truncated spectra are expressed as Eq. 2.3.3-1 below.

$$S_{FCE,b,d} = FFT[fftshift(I_{FCE,b,d})] \cdot dOPD_b^{ideal} \quad \text{Eq. 2.3.3-1}$$

where, $dOPD_b^{ideal}$ denotes the sampling interval for each band.

Then, FCE is calculated as Eq. 2.3.3-2 below.

$$FCE_{b,d} = \text{round} \left[\frac{\text{fit}_{S_{FCE,b,d}}^{phase}}{2\pi} \cdot FCE_{b,window} \right] \quad \text{Eq. 2.3.3-2}$$

After that, the effective points of the interferogram are trimmed based on Eq. 2.3.3-3 and Eq. 2.3.3-4.

Odd N: $ZPD_{pos,b,d} - \text{floor} \left(\frac{N}{2} \right)$ to $ZPD_{pos,b,d} + \text{floor} \left(\frac{N}{2} \right)$

$$I_{trim,b,d}^X[n] = I_{nlc,b,d}^X \left[ZPD_{pos,b,d} - \text{floor} \left(\frac{N}{2} \right) : ZPD_{pos,b,d} + \text{floor} \left(\frac{N}{2} \right) \right] \quad \text{Eq. 2.3.3-3}$$

Even N: $ZPD_{pos,b,d} - \left(\frac{N}{2}\right)$ to $ZPD_{pos,b,d} + \left(\frac{N}{2}\right) - 1$

$$I_{trim,b,d}^X[n] = I_{nlc,b,d}^X \left[ZPD_{pos,b,d} - \frac{N}{2} : ZPD_{pos,b,d} + \frac{N}{2} - 1 \right]$$

Eq. 2.3.3-4

Table 2.3.3-1. Effective sampling points (SWIR)

Band	Effective sampling points
B1P/S	153090
B2P/S	76545
B3P/S	76545

The ZPD position is usually the same. However, GOSAT experienced a ZPD shift under the low metrology signal condition. In that case, the ZPD position had been controlled with an offset. In other words, it was not a center of sampling points and created an offset interferogram. In this case, the weighing function for the interferogram is applied to maintain the quality of spectra. Fig. 2.3.3-2 shows a schematic view of the offset interferogram and weighing function. The offset interferogram creates zero values on one side in case of the ZPD position is replaced in the center of sampling points. Then these zero values must be removed from the interferogram. However, the interferogram size must be retained in order to maintain the spectral resolution. Therefore, information weighing of the opposite side for the interferogram must be doubled.

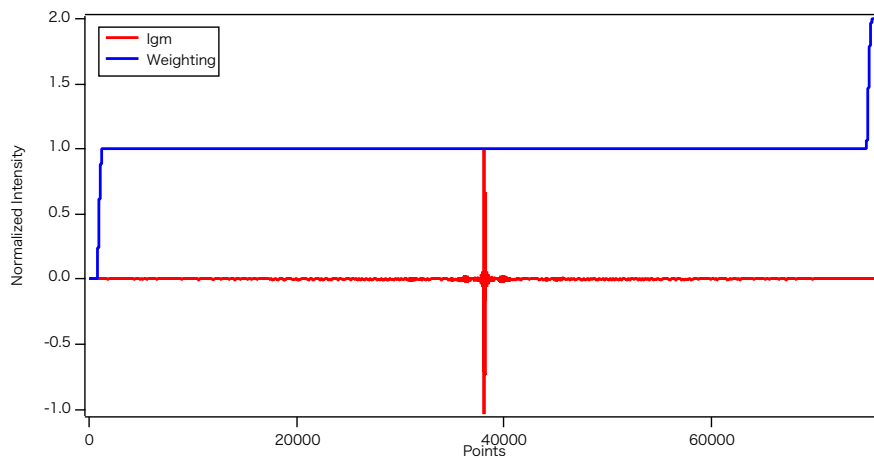


Fig. 2.3.3-2. Weighing function for offset interferogram

Eq. 2.3.3-5 expresses the weighing function for SWIR, where, $X_{zerofill,b}$ represents the zero interferogram region.

$$W_{SWIR_ZPD,b} = \begin{cases} 0 & , \quad \text{if } 0 \leq n \leq X_{zerofill,b} \\ F_{SWIR_ZPD_L} & , \quad \text{if } X_{zerofill,b} + 1 \leq n \leq X_{zerofill,b} + W_{smooth_SWIR,b} \\ 1 & , \quad \text{if } X_{zerofill,b} + W_{smooth_SWIR,b} + 1 \leq n \leq end - (X_{zerofill,b} + W_{smooth_SWIR,b}) \\ F_{SWIR_ZPD_R} & , \quad \text{if } end - (X_{zerofill,b} + W_{smooth_SWIR,b}) + 1 \leq n \leq end - X_{zerofill,b} \\ 2 & , \quad \text{if } end - X_{zerofill,b} + 1 \leq n \leq end \end{cases}$$

$$\begin{aligned}
F_{SWIR_ZPD_L} &= -0.5 \times \cos\left(\frac{\pi}{W_{smooth_SWIR,b}} \cdot (n - X_{zerofill,b})\right) + 0.5 \\
F_{SWIR_ZPD_R} &= 0.5 \times \cos\left(\frac{\pi}{W_{smooth_SWIR,b}} \cdot (n - (end - X_{zerofill,b} + 1))\right) + 1.5
\end{aligned}$$

Eq. 2.3.3-5

$W_{smooth_SWIR,b}$ denotes the transition region between the nominal interferogram and weighted interferogram. Then Eq. 2.3.3-6 expresses the weighted interferogram. Before processing the weighted interferogram, the DC components are removed.

$$I_{trim,b,d}^{X,AC,W}[n] = W_{SWIR_ZPD,b} \cdot I_{trim,b,d}^{X,AC}[n]$$

Eq. 2.3.3-6

In Eq. 2.3.3-7, the DC components are recovered.

$$I_{trim,b,d}^{X,W}[n] = I_{trim,b,d}^{X,AC,W}[n] + \frac{I_{trim,b,d}^X[N] - I_{trim,b,d}^X[1]}{N - 1} \cdot (n - 1) + I_{trim,b,d}^X[1]$$

Eq. 2.3.3-7

Finally, Eq. 2.3.3-8 defines the weighted interferogram.

$$I_{trim,b,d}^X = I_{trim,b,d}^{X,W}$$

Eq. 2.3.3-8

STEP_S2: Low frequency correction

Scene fluctuations during the observation period will create an artificial signal on spectra. These fluctuations generally appear in the low frequency region. The variation in radiance will be corrected based on low frequency correction. The low frequency region is assigned as S_{SWIR} cm^{-1} . First, the DC components are removed from the interferogram as expressed in Eq. 2.3.3-9.

$$I_{DC_off,b,d}^X[n] = I_{trim,b,d}^X[n] - \frac{I_{trim,b,d}^X[N] - I_{trim,b,d}^X[1]}{N - 1} \cdot (n - 1) - I_{trim,b,d}^X[1]$$

Eq. 2.3.3-9

Then, Fourier transform is applied as follows.

$$S_{b,d}^X[n] = FFT(I_{DC_off,b,d}^X[n])$$

Eq. 2.3.3-10

Low frequency components are extracted with the filter applied as expressed in Eq. 2.3.3-11.

$$F_{SWIR} = \begin{cases} \left(\frac{1 + \cos \frac{\pi \nu}{S_{SWIR}}} {2} \right)^{N_{SWIR}}, & \text{if } \nu < S_{SWIR} \\ 0, & \text{if } \nu \geq S_{SWIR} \end{cases}$$

Eq. 2.3.3-11

where,

ν : Wavenumber

S_{SWIR} : Cutoff frequency for SWIR bands

N_{SWIR} : Orders of filter

Then, Eq. 2.3.3-12 expresses the corresponded low frequency interferogram.

$$I_{smooth,b,d}^x(n) = Real\{IFFT(F \cdot S_{b,d}^X)\} + \frac{I_{trim,b,d}^x[N] - I_{trim,b,d}^x[1]}{N - 1} \cdot (n - 1) + I_{trim,b,d}^x[1]$$

Eq. 2.3.3-12

$I_{corr,b,d}^x(n)$, which is the radiance variation corrected interferogram, is presented as Eq. 2.3.3-13.

$$I_{corr,b,d}^x(n) = \frac{I_{trim,b,d}^x(n)}{I_{smooth,b,d}^x(n)} I_{smooth_mean,b,d}^x(ZPD_{pos,b,d})$$

Eq. 2.3.3-13

$$I_{smooth_mean,b,d}^x(ZPD_{pos,b,d}) = mean[I_{smooth,b,d}^x(ZPD_{pos,b,d} - LFC_{b>window} : ZPD_{pos,b,d} + LFC_{b>window})]$$

Eq. 2.3.3-14

STEP_S4: Phase correction

To correct the phase of spectra, Mertz methods are employed. The low spectral resolution spectra for processing phase parameter, $S_{Low,b,d}$ is calculated as Eq. 2.3.3-15.

$$x = \frac{n - \frac{N}{2}}{N} \cdot dOPD_b^{ideal}$$

$$Flt = e^{-\frac{x^2}{\sigma^2}}$$

$$S_{Low,b,d} = FFT[fftshift(Flt \cdot I_{SINUC,b,d})]$$

Eq. 2.3.3-15

where,

σ [cm]: Window side for gauss function

Original full interferogram $I_{SINUCl,b,d}$ is transformed to $S_{full,b,d}$ by applying Eq. 2.3.3-7.

$$S_{full,b,d} = FFT[fftshift(I_{SINUC,b,d})]$$

Eq. 2.3.3-16

Then, the phase-corrected spectra are processed with Eq. 2.3.3-17.

$$S_{b,d} = S_{full,b,d} \cdot \exp[-1i \cdot \text{angle}(S_{Low,b,d})] \cdot dOPD_b^{ideal}$$

Eq. 2.3.3-17

Eq. 2.3.3-18 describes the corresponded wavenumber.

$$\delta\sigma = \frac{1}{dOPD_b^{ideal} \cdot N}$$

Eq. 2.3.3-18

Fig. 2.3.3-3 and in Fig. 2.3.3-4 show typical examples for spectra and phase, respectively.

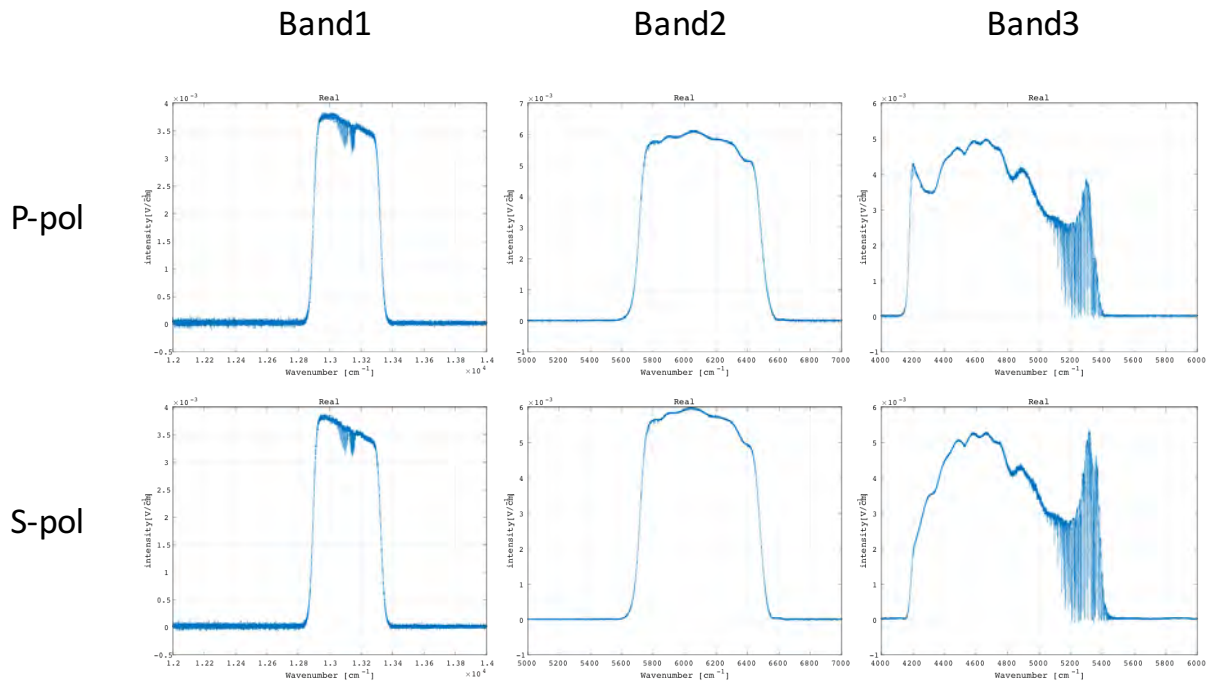


Fig. 2.3.3-3. Spectra

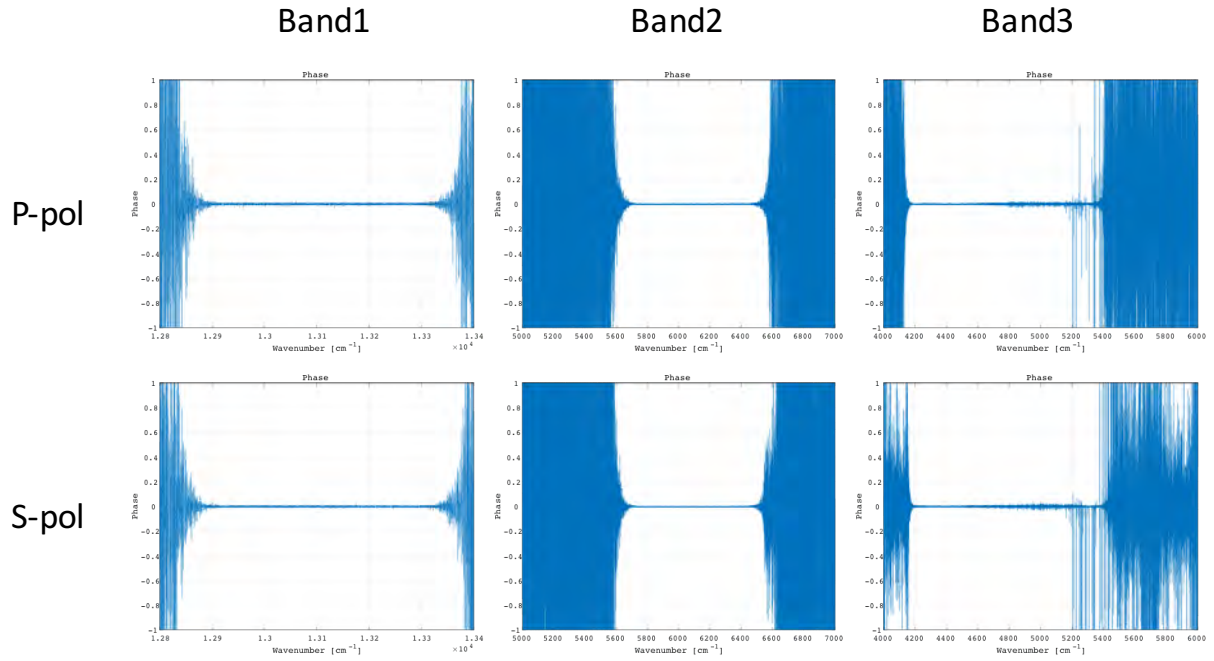


Fig. 2.3.3-4. Phase

STEP_S6: Processing for radiance spectra

The unit of $S_{b,d}$ is ν/cm^{-1} . To make a radiance spectrum, $S_{b,d}$ multiplied radiance conversion factor CNV_b as well as the time-dependent degradation factor $Y(\nu, t)$. Then, Eq. 2.3.3-19 expresses the radiance spectra at time t .

$$Rad_{b,d}(\nu, t) = \frac{CNV_b \cdot S_{b,d}(\nu, t)}{Y(\nu, t)}$$

Eq. 2.3.3-19

2.3.4 Processing for Band 4-5 spectra

This section describes the processing method for TIR (bands 4 and 5). In contrast to SWIR processing, TIR processing requires not only nadir observation spectra but also calibration spectra, such as deep space calibration and black body calibration. The latest calibration spectra against nadir observation will be selected.

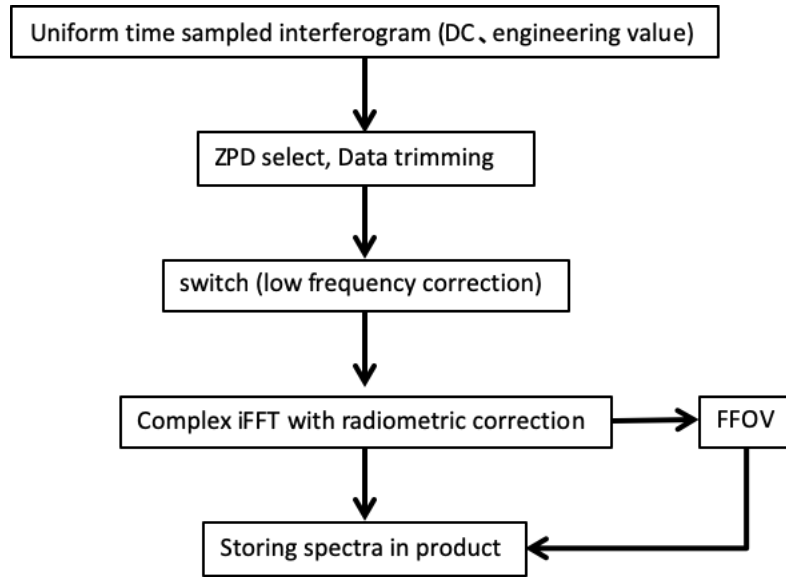


Fig. 2.3.4-1. Processing flow for Band 4 and 5

STEP_T1: Data trimming

The data trimming method is the same as for SWIR. Optical and mechanical ZPD positions are generally not equal. To identify the optical ZPD position, the ZPD position is processed as follows: First, the maximum signal points around the sampling center are detected. Second, fringe count error (FCE) is calculated and applied for correction of the ZPD position.

FCE is processed with a truncated interferogram around the maximum signal position ($I_{nlc,b,d}^X$) with truncation size ($FCE_{b,window}$). Then, Eq. 2.3.4-1 expresses the truncated spectra.

$$S_{FCE,b,d} = FFT[fftshift(I_{FCE,b,d})] \cdot dOPD_b^{ideal} \quad \text{Eq. 2.3.4-1}$$

where, $dOPD_b^{ideal}$ denotes the sampling interval for each band.

Then, $FCE_{b,d}$ is calculated as Eq. 2.3.4-2.

$$FCE_{b,d} = \text{round} \left[\frac{\text{fit}_{S_{FCE,b,d}}^{phase}}{2\pi} \cdot FCE_{b,window} \right] \quad \text{Eq. 2.3.4-2}$$

After that, the effective points of the interferogram are trimmed based on Eq. 2.3.4-3 and Eq. 2.3.4-4 below.

Odd N: $ZPD_{pos,b,d} - \text{floor} \left(\frac{N}{2} \right)$ to $ZPD_{pos,b,d} + \text{floor} \left(\frac{N}{2} \right)$

$$I_{trim,b,d}^X[n] = I_{nlc,b,d}^X \left[ZPD_{pos,b,d} - \text{floor} \left(\frac{N}{2} \right) : ZPD_{pos,b,d} + \text{floor} \left(\frac{N}{2} \right) \right] \quad \text{Eq. 2.3.4-3}$$

Even N: $ZPD_{pos,b,d} - \left(\frac{N}{2}\right)$ to $ZPD_{pos,b,d} + \left(\frac{N}{2}\right) - 1$

$$I_{trim,b,d}^X[n] = I_{nlc,b,d}^X \left[ZPD_{pos,b,d} - \frac{N}{2} : ZPD_{pos,b,d} + \frac{N}{2} - 1 \right]$$

Eq. 2.3.4-4

Table 2.3.4-1. Effective sampling points(TIR)

Band	Effective sampling points
B4	38250
B5	38250

In the case of ZPD offset operation, the processing procedure is the same as SWIR. Fig. 2.3.4-2 shows the schematic weighing function.

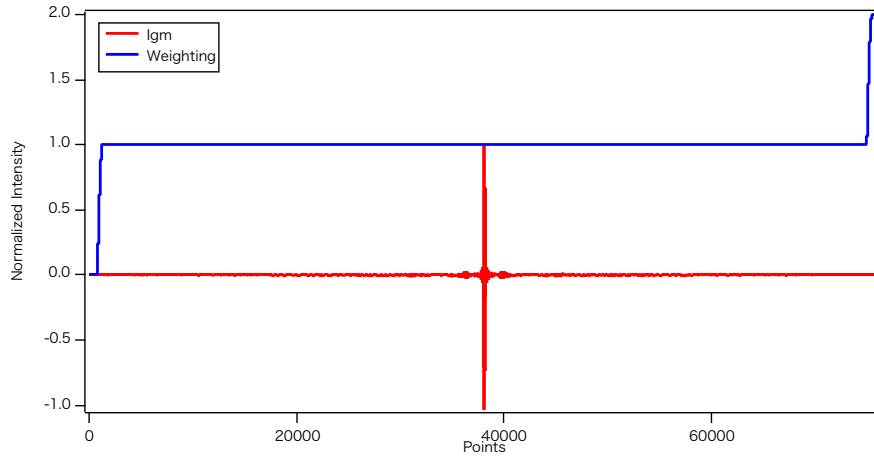


Fig. 2.3.4-2. Weighting function for offset interferogram

Eq. 2.3.4-5 expresses the weighting function for TIR interferogram, where, $X_{zerofill,b}$ denotes the zero interferogram region.

$$W_{TIR_ZPD,b} = \begin{cases} 0 & , \quad \text{if } 0 \leq n \leq X_{zerofill,b} \\ F_{TIR_ZPD_L} & , \quad \text{if } X_{zerofill,b} + 1 \leq n \leq X_{zerofill,b} + W_{smooth_TIR,b} \\ 1 & , \quad \text{if } X_{zerofill,b} + W_{smooth_TIR,b} + 1 \leq n \leq end - (X_{zerofill,b} + W_{smooth_TIR,b}) \\ F_{TIR_ZPD_R} & , \quad \text{if } end - (X_{zerofill,b} + W_{smooth_TIR,b}) + 1 \leq n \leq end - X_{zerofill,b} \\ 2 & , \quad \text{if } end - X_{zerofill,b} + 1 \leq n \leq end \end{cases}$$

$$F_{TIR_ZPD_L} = -0.5 \times \cos \left(\frac{\pi}{W_{smooth_TIR}} \cdot (n - X_{zerofill,b}) \right) + 0.5$$

$$F_{TIR_ZPD_R} = 0.5 \times \cos \left(\frac{\pi}{W_{smooth_TIR}} \cdot (n - (end - X_{zerofill,b} + 1)) \right) + 1.5$$

Eq. 2.3.4-5

$W_{smooth_TIR,b}$ denotes the transition region between the nominal interferogram and weighted interferogram. Eq. 2.3.4-6 expresses the weighted interferogram. Prior to processing of the weighted interferogram, the DC components are removed.

$$I_{trim,b,d}^{X,AC,W}[n] = W_{SWIR_ZPD,b} \cdot I_{trim,b,d}^{X,AC}[n] \quad \text{Eq. 2.3.4-6}$$

In Eq. 2.3.4-7, the DC components are recovered.

$$I_{trim,b,d}^{X,W}[n] = I_{trim,b,d}^{X,AC,W}[n] + \frac{I_{trim,b,d}^X[N] - I_{trim,b,d}^X[1]}{N-1} \cdot (n-1) + I_{trim,b,d}^X[1] \quad \text{Eq. 2.3.4-7}$$

Finally, Eq. 2.3.4-8 defines the weighted interferogram.

$$I_{trim,b,d}^X = I_{trim,b,d}^{X,W} \quad \text{Eq. 2.3.4-8}$$

STEP_T2: Low frequency correction

As described in the SWIR section, the TIR interferogram is also corrected for the low frequency radiance jitter. For TIR bands, the low frequency region is assigned as $S_{TIR} \text{ cm}^{-1}$, with the DC components first being removed from the interferogram as expressed in Eq. 2.3.4-9.

$$I_{DC_off,b,d}^X[n] = I_{trim,b,d}^X[n] - \frac{I_{trim,b,d}^X[N] - I_{trim,b,d}^X[1]}{N-1} \cdot (n-1) - I_{trim,b,d}^X[1] \quad \text{Eq. 2.3.4-9}$$

Then, Fourier transform is applied as follows:

$$S_{b,d}^X[n] = FFT(I_{DC_off,b,d}^X[n]) \quad \text{Eq. 2.3.4-10}$$

Low frequency components are extracted with the filter applied, as expressed in Eq. 2.3.4-11.

$$F_{TIR} = \begin{cases} \left(\frac{1 + \cos \frac{\pi \nu}{S_{TIR}}}{2} \right)^{N_{TIR}}, & \text{if } \nu < S_{TIR} \\ 0, & \text{if } \nu \geq S_{TIR} \end{cases} \quad \text{Eq. 2.3.4-11}$$

where,

ν : Wavenumber

S_{SWIR} : Cutoff frequency for TIR bands

N_{SWIR} : Orders of filter

Eq. 2.3.4-12 expresses the corresponded low frequency interferogram.

$$I_{smooth,b,d}^x(n) = Real\{IFFT(F \cdot S_{b,d}^x)\} + \frac{I_{trim,b,d}^x[N] - I_{trim,b,d}^x[1]}{N - 1} \cdot (n - 1) + I_{trim,b,d}^x[1]$$

Eq. 2.3.4-12

Eq. 2.3.4-13 expresses $I_{corr,b,d}^x(n)$, which is radiance variation corrected interferogram.

$$I_{corr,b,d}^x(n) = \frac{I_{trim,b,d}^x(n)}{I_{smooth,b,d}^x(n)} I_{smooth_mean,b,d}^x(ZPD_{pos,b,d})$$

Eq. 2.3.4-13

$$I_{smooth_mean,b,d}^x(ZPD_{pos,b,d}) = mean[I_{smooth,b,d}^x(ZPD_{pos,b,d} - LFC_{b,window} : ZPD_{pos,b,d} + LFC_{b,window})]$$

Eq. 2.3.4-14

STEP_T4: Complex radiance

Radiance spectra $L_{b,d}^{obs}$ is processed with nadir observation complex spectra, blackbody complex spectra, and deep space complex spectra. $L_{b,d}^{obs}$ is expressed as Eq. 2.3.4-15

For the version of 102102 processing, method 1 processing below is applied. For the version of 200200 processing, the method 2 is applied.

Method1:

$$L_{b,d}^{obs} = \left[\frac{S_{b,d}^{obs} - S_{b,d}^{ds}}{\eta S_{b,d}^{ict} - S_{b,d}^{ds}} - \frac{\epsilon^{obs} L_{b,d}^{m_obs} - \epsilon^{ds} L_{b,d}^{m_ds}}{(1 - \epsilon^{ds}) \cdot \epsilon^{ict} \cdot L_{b,d}^{ict} + \epsilon^{ds} (L_{b,d}^{m_ict} - L_{b,d}^{m_ds})} \right] \cdot \frac{(1 - \epsilon^{ds}) \cdot \epsilon^{ict} \cdot L_{b,d}^{ict} + \epsilon^{ds} (L_{b,d}^{m_ict} - L_{b,d}^{m_ds})}{(1 - \epsilon^{obs})}$$

Eq. 2.3.4-15

Wavenumber σ is shown in Eq. 2.3.4-16 below.

$$\delta\sigma = \frac{1}{dOPD_b^{ideal} \cdot N}$$

Eq. 2.3.4-16

where.

$L_{b,d}^{obs}$: Calibrated Earth scene radiance

$L_{b,d}^{ict}$: Blackbody radiance

$S_{b,d}^{obs}$: Raw complex spectra for Earth scene

$S_{b,d}^{ict}$: Raw complex spectra for blackbody scene

$S_{b,d}^{ds}$: Raw complex spectra for deep space scene

$L_{b,d}^{m,obs}$: Scan mirror radiance calculated from the mirror temperature measured while viewing the Earth scene.

$L_{b,d}^{m,ds}$: Scan mirror radiance calculated from the mirror temperature measured while viewing the deep space scene.

$L_{b,d}^{m,ict}$: Scan mirror radiance calculated from the mirror temperature measured while viewing the blackbody scene.

ε^{obs} : Scan mirror emissivity when viewing the Earth scene

ε^{ds} : Scan mirror emissivity when viewing the deep space scene

ε^{ict} : Blackbody emissivity

η : Sensitivity correction parameter for complex blackbody spectra.

N : Sampling points.

$S_{b,d}^{ds}$, $S_{b,d}^{ict}$ and $S_{b,d}^{obs}$ are expressed as follows:

$$S_{b,d}^{ds} = FFT[fftshift(I_{b,d}^{ds})] \cdot dOPD_b^{ideal} \quad \text{Eq. 2.3.4-17}$$

$$S_{b,d}^{ict} = FFT[fftshift(I_{b,d}^{ict})] \cdot dOPD_b^{ideal} \quad \text{Eq. 2.3.4-18}$$

$$S_{b,d}^{obs} = FFT[fftshift(I_{b,d}^{obs})] \cdot dOPD_b^{ideal} \quad \text{Eq. 2.3.4-19}$$

$L_{b,d}^{ict}$, $L_{b,d}^{ds}$, $L_{b,d}^{m,obs}$, $L_{b,d}^{m,ds}$, $L_{b,d}^{m,ict}$ are calculated with plank row equations as follows:

$$L_{b,d}^{ict}(\sigma, T_{ict_ave}) = \frac{\frac{2}{100} \cdot c \cdot h \cdot (100 \cdot c \cdot \sigma)^3}{c^2 \cdot \left\{ \exp\left(100 \cdot c \cdot \sigma \cdot \frac{h}{k \cdot T_{ict_ave}}\right) - 1 \right\}} \quad \text{Eq. 2.3.4-20}$$

$$L_{b,d}^{ds}(\sigma, T_{ds}) = \frac{\frac{2}{100} \cdot c \cdot h \cdot (100 \cdot c \cdot \sigma)^3}{c^2 \cdot \left\{ \exp\left(100 \cdot c \cdot \sigma \cdot \frac{h}{k \cdot T_{ds}}\right) - 1 \right\}} \quad \text{Eq. 2.3.4-21}$$

$$L_{b,d}^{m,obs}(\sigma, T_{m,obs}) = \frac{\frac{2}{100} \cdot c \cdot h \cdot (100 \cdot c \cdot \sigma)^3}{c^2 \cdot \left\{ \exp\left(100 \cdot c \cdot \sigma \cdot \frac{h}{k \cdot T_{m,obs}}\right) - 1 \right\}} \quad \text{Eq. 2.3.4-22}$$

$$L_{b,d}^{m,ds}(\sigma, T_{m,ds}) = \frac{\frac{2}{100} \cdot c \cdot h \cdot (100 \cdot c \cdot \sigma)^3}{c^2 \cdot \left\{ \exp\left(100 \cdot c \cdot \sigma \cdot \frac{h}{k \cdot T_{m,ds}}\right) - 1 \right\}} \quad \text{Eq. 2.3.4-23}$$

$$L_{b,d}^{m,ict}(\sigma, T_{m,ict}) = \frac{\frac{2}{100} \cdot c \cdot h \cdot (100 \cdot c \cdot \sigma)^3}{c^2 \cdot \left\{ \exp\left(100 \cdot c \cdot \sigma \cdot \frac{h}{k \cdot T_{m,ict}}\right) - 1 \right\}}$$

Eq. 2.3.4-24

σ : Wavenumber (cm^{-1})

$T_{ict,ave}$: Averaged blackbody temperature (K)

T_{ds} : Temperature of deep space viewing (K)

$T_{m,ds}$: Scan mirror temperature during deep space viewing (K)

$T_{m,ict}$: Scan mirror temperature during blackbody viewing (K)

$T_{m,obs}$: Scan mirror temperature during earth scene viewing (K)

c : Light speed (2.99792458×10^8 [m/s])

h : Plank constant ($6.62606876 \times 10^{-34}$ [J·s])

k : Boltzmann constant ($1.3806503 \times 10^{-23}$ [J/K])

Method 2:

$$L_{b,d}^{obs} = \left[\frac{S_{b,d}^{obs} - S_{b,d}^{ds}}{S_{b,d}^{ict} - S_{b,d}^{ds}} \right] \cdot \left[\frac{(p_2^2(\sigma) + q_2^2(\sigma))(p_1^2(\sigma) + q_1^2(\sigma)) - (p_2^2(\sigma) - q_2^2(\sigma))(p_1^2(\sigma) - q_1^2(\sigma))}{(p_2^2(\sigma) + q_2^2(\sigma))(p_1^2(\sigma) + q_1^2(\sigma)) + (p_2^2(\sigma) - q_2^2(\sigma))(p_1^2(\sigma) - q_1^2(\sigma))} \right] B_{b,d}^{ict} + \left[\frac{2(p_2^2(\sigma) - q_2^2(\sigma))(p_1^2(\sigma) - q_1^2(\sigma))}{(p_2^2(\sigma) + q_2^2(\sigma))(p_1^2(\sigma) + q_1^2(\sigma)) + (p_2^2(\sigma) - q_2^2(\sigma))(p_1^2(\sigma) - q_1^2(\sigma))} \right] L_{b,d}^{m,obs}$$

Eq. 2.3.4-25

$$B_b^{ict}[n] = C_b^{ict}[n] + C_b^{ict_baffle}[n] + C_b^{SAA_str}[n] + C_b^{OMA}[n] + C_b^{BS}[n]$$

Eq. 2.3.4-26

$$C_b^{ict}[n] = \varepsilon_b^{ict} \cdot L_b(\sigma_b[n], T^{ict})$$

Eq. 2.3.4-27

$$C_b^{ict_baffle}[n] = (1 - \varepsilon_b^{ict}) \cdot \varepsilon_b^{ict_baffle} \cdot A^{ict_baffle} \cdot L_b(\sigma_b[n], T^{SSA+Y})$$

Eq. 2.3.4-28

$$C_b^{SAA_str}[n] = (1 - \varepsilon_b^{ict}) \cdot \varepsilon_b^{SAA_str} \cdot A^{SAA_str} \cdot L_b(\sigma_b[n], T^{SSA-Y})$$

Eq. 2.3.4-29

$$C_b^{OMA}[n] = (1 - \varepsilon_b^{ict}) \cdot (1 - \varepsilon_b^{scanner_mirror}) \cdot \varepsilon_b^{OMA} \cdot (A^{OMA}) \cdot L_b(\sigma_b[n], T^{IOA+Z})$$

Eq. 2.3.4-30

$$C_b^{BS}[n] = (1 - \varepsilon_b^{ict}) \cdot (1 - \varepsilon_b^{scanner_mirror}) \cdot A^{BS} \cdot L_b(\sigma_b[n], T^{BS})$$

Eq. 2.3.4-31

$$A^{ict_baffle} + A^{SAA_str} + A^{OMA} + A^{BS} = 1$$

Eq. 2.3.4-32

p_1^2, q_1^2 : Reflection of scanner mirror $p_1^2 = R_p(AT_{ang}, CT_{ang})$, $q_1^2 = R_s(AT_{ang}, CT_{ang})$

p_2^2, q_2^2 : Trannsmittance of both p and s polarization $p_2^2 = T_p$, $q_2^2 = T_s$

ε^{ict} : Blackbody emissivity

$L_b(\sigma_b[n], T^{ict})$: Radiance for the blackbody temperature T^{ict} against wavenumber $\sigma_b[n]$

$\varepsilon_b^{ict_baffle}$: Emissivity of baffle

A^{ict_baffle} : View factor of baffle

$L_b(\sigma_b[n], T^{SSA+Y})$: Radiance for the temperature of SSA+Y assy: T^{SSA+Y} against wavenumber $\sigma_b[n]$

$\varepsilon_b^{SAA_str}$: Emissivity of SAA assy

A^{SAA_str} : View factor of SAA

$L_b(\sigma_b[n], T^{SSA-Y})$: Radiance for the temperature of SSA-Y assy: T^{SSA-Y} against wavenumber $\sigma_b[n]$

ε_b^{OMA} : Missivity of OMA assy

A^{OMA} : View factor of OMA

$L_b(\sigma_b[n], T^{IOA+Z})$: Radiance for the temperature of IOA+Z assy: T^{IOA+Z} against $\sigma_b[n]$

A^{BS} : View factor of BS

$L_b(\sigma_b[n], T^{BS})$: Radiance for the temperature of T^{BS} against $\sigma_b[n]$

$\varepsilon_b^{scanner_mirror}$: Emissivity of of scanner mirror

$L_b^{m_obs}(\sigma_b[n], T^{m_obs})$: Radiance for the temperature of scanner mirror: T^{m_obs} against $\sigma_b[n]$

Wavenumber σ is defined as follows:

$$\delta\sigma = \frac{1}{dOPD_b^{ideal} \cdot N}$$

Eq. 2.3.4-33

N : Sampling points.

$T_{b,d}^{obs}$ is defined by $L_{b,d}^{obs}$

$$T_{b,d}^{obs} = \frac{C2 \cdot \sigma}{\log\left(\frac{C1 \cdot \sigma^3}{\pi \cdot real(L_{b,d}^{obs})}\right) + 1}$$

Eq. 2.3.4-34

where,

$$C1 = 3.7418e^{-12} [cm^2W]$$

$$C2 = 1.4388 [cm K]$$

When $p_1^2 = q_1^2, p_2^2 = q_2^2$, Eq. 2.3.4-15 is simplified as follows:

$$L_{b,d}^{obs} = \left[\frac{S_{b,d}^{obs} - S_{b,d}^{ds}}{S_{b,d}^{ict} - S_{b,d}^{ds}} \right] \cdot B_b^{ict}$$

Eq. 2.3.4-35

Where, $S_{b,d}^{ds}$, $S_{b,d}^{ict}$ and $S_{b,d}^{obs}$ are expressed as follows:

$$S_{b,d}^{ds} = FFT[fftshift(I_{b,d}^{ds})] \cdot dOPD_b^{ideal}$$

Eq. 2.3.4-36

$$S_{b,d}^{ict} = FFT[fftshift(I_{b,d}^{ict})] \cdot dOPD_b^{ideal}$$

Eq. 2.3.4-37

$$S_{b,d}^{obs} = FFT[fftshift(I_{b,d}^{obs})] \cdot dOPD_b^{ideal}$$

Eq. 2.3.4-38

$L_b(\sigma_b[n], T)$ is defined as follows;

$$L_{b,d}(\sigma, T) = \frac{\frac{2}{100} \cdot c \cdot h \cdot (100 \cdot c \cdot \sigma)^3}{c^2 \cdot \left\{ \exp\left(100 \cdot c \cdot \sigma \cdot \frac{h}{k \cdot T}\right) - 1 \right\}}$$

Eq. 2.3.4-39

σ : Wavenumber (cm^{-1})

T_{ict_ave} : Averaged black body temperature (K)

c : Light speed (2.99792458×10^8 [m/s])

h : Plank constant ($6.62606876 \times 10^{-34}$ [J·s])

k : Boltzmann constant ($1.3806503 \times 10^{-23}$ [J/K])

Fig. 2.3.4-3 illustrates ε^{ict} .

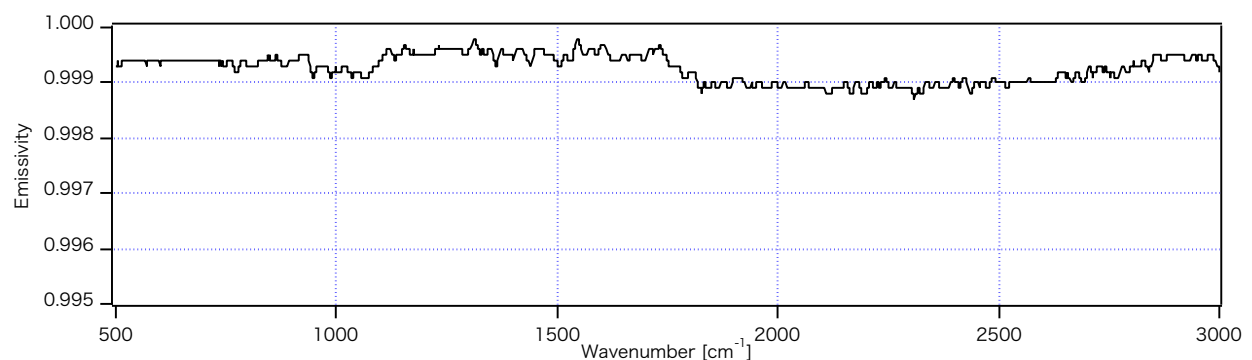


Fig. 2.3.4-3. Blackbody emissivity

ε^{obs} , ε^{ds} and $\varepsilon^{scanner_mirror}$ are calculated based on scan mirror complex reflectivity. Eq. 2.3.4-40 to Eq. 2.3.4-46 process the scanner reflectance. Where AT_{ang} and CT_{ang} are telemetry values that are transmitted to the ground.

$$\cos\theta_i = \frac{\cos(CT_{ang}) \cdot \sin(AT_{ang}) + \cos(AT_{ang})}{\sqrt{2}}$$

Eq. 2.3.4-40

$$\sin^2\theta_i = 1 - \cos^2\theta_i$$

Eq. 2.3.4-41

$$r_p(m, \theta_i) = \frac{m^2 \cos\theta_i - \sqrt{m^2 - \sin^2\theta_i}}{m^2 \cos\theta_i + \sqrt{m^2 - \sin^2\theta_i}}$$

Eq. 2.3.4-42

$$r_s(m, \theta_i) = \frac{\cos\theta_i - \sqrt{m^2 - \sin^2\theta_i}}{\cos\theta_i + \sqrt{m^2 - \sin^2\theta_i}}$$

Eq. 2.3.4-43

$$R_p(AT_{ang}, CT_{ang}) = r_p(m, \theta_i) \cdot r_p^*(m, \theta_i) = \frac{|m^2 \cos\theta_i - \sqrt{m^2 - \sin^2\theta_i}|^2}{|m^2 \cos\theta_i + \sqrt{m^2 - \sin^2\theta_i}|^2}$$

Eq. 2.3.4-44

$$R_s(AT_{ang}, CT_{ang}) = r_s(m, \theta_i) \cdot r_s^*(m, \theta_i) = \frac{|\cos\theta_i - \sqrt{m^2 - \sin^2\theta_i}|^2}{|\cos\theta_i + \sqrt{m^2 - \sin^2\theta_i}|^2}$$

Eq. 2.3.4-45

$$\delta(AT_{ang}, CT_{ang}) = \tan^{-1} \left(\frac{Im[r_p(m, \theta_i)r_s^*(m, \theta_i)]}{Re[r_p(m, \theta_i)r_s^*(m, \theta_i)]} \right)$$

Eq. 2.3.4-46

where,

m : Complex reflectivity in wavelength

θ_i : Variables

r_s, r_p : Complex variables

R_s, R_p : Reflectance for p and s polarization.

are presented in Fig. 2.3.4-4 shows R_s, R_p in the case of $AT_{ang} = 0, CT_{ang} = 0$.

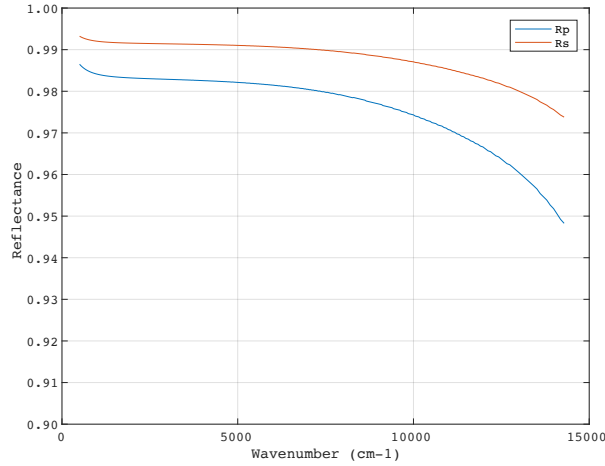


Fig. 2.3.4-4. Scanner reflectivity

Finally, scanner emissivity is calculated by applying Eq. 2.3.4-47.

$$\varepsilon^{xx}(AT_{ang}, CT_{ang}) = 1 - \frac{1}{2} [R_p(AT_{ang}, CT_{ang}) + R_s(AT_{ang}, CT_{ang})]$$

Eq. 2.3.4-47

where,

xx : Earth scene viewing or deep space viewing

Adjustment of ZPD position between observation, deep space calibration, and blackbody calibration

Usually, the optical ZPD position is identified and not time dependent. However, lessons learned from GOSAT show that GOSAT type FTS may change the ZPD position, especially in the TIR region due to the balance between incident and background radiation. To identify the proper ZPD position, the ZPD adjustment approach is applied to the version 102102 algorithm. This is a simple method of comparing the real part and imaginary part of calibration spectra. At the proper ZPD position, the imaginary part is minimized.

STEP_T5: Apodization

Finite field of view correction is applied for Earth scene observation spectra. In parallel, it can be applicable to the apodization function. Gauss, Norton-Beer, and boxcar functions are selectable in the processing. Eq. 2.3.4-48 expresses the Norton-Beer function, and Table 2.3.4-2 lists the coefficient.

$$NB\left(\frac{\delta}{L}\right) = \sum_{i=0}^n C_i \left(1 - \left(\frac{\delta}{L}\right)^2\right)^i,$$

$$\text{where, } \sum_{i=0}^n C_i = 1, n = 4$$

Eq. 2.3.4-48

where, δ is expressed as follows:

$$-laser_{WL} \times \frac{38250}{2} \leq \delta \leq laser_{WL} \times \frac{38250}{2}$$

Table 2.3.4-2. Coefficients of the Norton-Beer function

Function	C0	C1	C2	C3	C4
Weak	0.384093	-0.087577	0.703484	0	0
Medium	0.152442	-0.136176	0.983734	0	0
Strong	0.045335	0	0.554883	0	0.399782

Eq. 2.3.4-49 expresses the Gauss function, where, σ is full width and half maximum, and N denotes sample points.

$$x = \frac{n - \frac{N}{2}}{N}$$

$$Gauss = e^{-\frac{x^2}{\sigma^2}}$$

Eq. 2.3.4-49

Eq. 2.3.4-50 expresses the boxcar function, where, x is the optical path difference, and L is the maximum optical path difference.

$$\prod(x) = 1, \quad |x| \leq L$$

$$\prod(x) = 0, \quad |x| > L$$

Eq. 2.3.4-50

The apodization function F_{apo} is selectable. Apodized spectra are expressed as $S_{b,d,obs}^{apo}$.

$$S_{b,d,obs}^{apo} = FFT^{-1} \left\{ F_{apo} \left[FFT \left(fftshift(L_{b,d}^{obs}) \right) \right] \right\}$$

Eq. 2.3.4-51

To reduce the out-of-band noise, the filter (expressed in Eq. 2.3.4-52) is applied for apodized spectra.

$$F_{FFOV} = \begin{cases} 0, & \text{if } 0 \leq n < \nu_{L1} - F_{width} \\ \left(\frac{1 + \cos \frac{\pi(n - (\nu_{L1} - F_{width}))}{F_{width}}}{2} \right)^{N_{FFOV}}, & \text{if } \nu_{L1} - F_{width} \leq n < \nu_{L1} \\ 1, & \text{if } \nu_{L1} \leq n < \nu_{H1} \\ \left(\frac{1 - \cos \frac{\pi(n - \nu_{H1})}{F_{width}}}{2} \right)^{N_{FFOV}}, & \text{if } \nu_{H1} \leq n < \nu_{H1} + F_{width} \\ 0, & \text{if } \nu_{H1} + F_{width} \leq n < \nu_{L2} - F_{width} \\ \left(\frac{1 + \cos \frac{\pi(n - (\nu_{L2} - F_{width}))}{F_{width}}}{2} \right)^{N_{FFOV}}, & \text{if } \nu_{L2} - F_{width} \leq n < \nu_{L2} \\ 1, & \text{if } \nu_{L2} \leq n < \nu_{H2} \\ \left(\frac{1 - \cos \frac{\pi(n - \nu_{H2})}{F_{width}}}{2} \right)^{N_{FFOV}}, & \text{if } \nu_{H2} \leq n < \nu_{H2} + F_{width} \\ 0, & \text{if } \nu_{H2} + F_{width} \leq n < end \end{cases}$$

Eq. 2.3.4-52

where,

ν : Wavenumber,

F_{width} : Roll-off window size

N_{FFOV} : Order of roll-off filter

STEP_T6: Finite FOV correction

Finite FOV correction is performed using Eq. 2.3.4-53.

$$I_V^m(x) = \frac{1}{2\pi} \int d\nu e^{i2\pi x \nu} \frac{\sin \left[2\pi x \nu \left(\frac{b^2}{4} \right) \right]}{2\pi x \nu \left(\frac{b^2}{4} \right)} S_{b,d,obs}^{apo}(\nu, d)$$

Eq. 2.3.4-53

where,

ν : Wavenumber

x : Optical path difference

d : Scan direction

b : Half angle of FOV $b = \frac{15.8}{2} \times 10^{-3} [rad]$

$I_V^m(x)$: FFOV corrected interferogram

$S_{b,d,obs}^{apo}(\nu, d)$: Apodised spectra

Finally, Eq. 2.3.4-56 expresses FFOV corrected spectra with correction terms.

$$I_v^m = FFT\{S(v)\} - \frac{\left[2\pi\left(\frac{b^2}{4}\right)\right]^2}{3!} x^2 FFT\{v^2 S(v)\} + \frac{\left[2\pi\left(\frac{b^2}{4}\right)\right]^4}{5!} x^4 FFT\{v^4 S(v)\} + O\left[\left(\frac{b^2}{4}\right)^6\right]$$

Eq. 2.3.4-54

$$\Delta C_v^m \cong \frac{\left[2\pi\left(\frac{b^2}{4}\right)\right]^2}{3!} FFT^{-1}[x^2 FFT(v^2 C_v^m)] - \frac{\left[2\pi\left(\frac{b^2}{4}\right)\right]^4}{5!} FFT^{-1}[x^4 FFT(v^4 C_v^m)]$$

Eq. 2.3.4-55

ΔC_v^m express the correction term for FFOV corrected spectra.

$$S_{b,d,obs}^{FFOV}(v, d) = S_{b,d,obs}^{apo}(v, d) + \Delta C_v^m$$

Eq. 2.3.4-56

Appendix 1: Sensitivity degradation correction

Sensitivity degradation is expressed with two terms; one is wavenumber-dependent term and the other is time-dependent term. Eq. 2.3.4-57 and Eq. 2.3.4-58 describe these terms, respectively. Time t is originated as 2019/02/05 00:00:00.

Wavenumber dependence

$$Y(v) = a_1 + a_2 v + a_3 v^2 + a_4 v^3$$

Eq. 2.3.4-57

Time dependence

$$Y(t) = d + e \cdot \exp\left[-\frac{t}{f}\right]$$

Eq. 2.3.4-58

Appendix 2: Characteristics of scanner reflectance

Scanner reflectance is processed by applying complex refraction measured with a witness sample. Measurement is performed in steps of 5 nm. Spline interpolation is employed to process the reflectance against a specific wavenumber.

2.3.5 Quality control

Spectral quality is controlled to compare the values of selected items with the reference values. If the observed values exceed the reference values, a warning flag is added to L1 products. The temperature between Celsius and Kelvin is employed as $t[^\circ\text{C}] = T[\text{K}] - 273.15$.

i. Observation time

Observation time is assigned as the observation start time (rising time of the sampling window) plus half of observation duration (fixed value: 2.012sec).

ii. Interferogram quality control

In the interferogram domain, saturation, low frequency variation of the interferogram, and speed fluctuations are checked. If these values exceed the reference values, a poor flag is added to the product. If these values match the reference values, a good flag is added.

iii. Spectral quality control

The averaged real part and imaginary part of the out-of-band region are compared with the reference values. If the measured values exceeds the reference values, a poor flag is added to the product. Table 2.3.5-1 lists the out-of-band and in-band regions.

Table 2.3.5-1. in-band and out-of-band regions

Band	Out-of-band region (real part) [cm ⁻¹]	Reference value (real part)	In-band region (imag. part) [cm ⁻¹]	Reference value (imag. part)	In-band region (real part) [cm ⁻¹]
B1	12450-12550 (Low) 13650-13750 (High)	10 ⁻⁴	12950-13250	10 ⁻²	12950-13250
B2	4800-4900 (Low) 7000-7100 (High)	10 ⁻⁵	5900-6400	10 ⁻²	5900-6400
B3	3800-3900 (Low) 5700-5800 (High)	10 ⁻⁵	4200-5200	10 ⁻²	4200-5200
B4	988-1038 (Low) 1950-2000 (High)	10 ⁻⁴	1188-1800	10 ⁻²	1188-1800
B5	500-600 (Low) 1288-1388 (High)	10 ⁻⁶	700-1188	10 ⁻²	700-1188

As a reference, simple SNR is expressed in Eq. 2.3.5-1 below.

$$Simple\ SNR = \frac{\text{max value in band}}{\text{average(Lowside, stdev. for outband + Highside, stdev, for outband)}}$$

Eq. 2.3.5-1

iv. Stability of image motion compensation

AT and CT motor angles are sampled with 100Hz. A total of 402 samples is recorded during one observation, and transmitted to the ground. Observed motor angles and commanded angles are directly compared for each sampled point, to check the stability of image motion compensation. If the difference is wider than the reference values, a warning flag is recorded in the product.

v. Observation point

The observation points of FTS-2 is fully programmable. All of observation points are identified with XYZ in WGS84 coordination. The root means square value between observed XYZ and commanded XYZ, which is

expressed in Eq. 2.3.5-2, presents the pointing accuracy against the observation plan. $Diff_{xyz}$ is stored in L1 product as part of reference value.

$$Diff_{xyz} = \sqrt{(X_{obs} - X_{plan})^2 + (Y_{obs} - Y_{plan})^2 + (Z_{obs} - Z_{plan})^2}$$

Eq. 2.3.5-2

2.3.6 Observation time

Satellite time

Eq. 2.3.6-1 defines satellite time.

$$\text{Satellite time (s)} = \text{GPS time(s)} - 1,041,033,615(\text{s})$$

Eq. 2.3.6-1

2.3.7 Processing for line of scene

Fig. 2.3.7-1 shows a schematic view of scanner coordination.

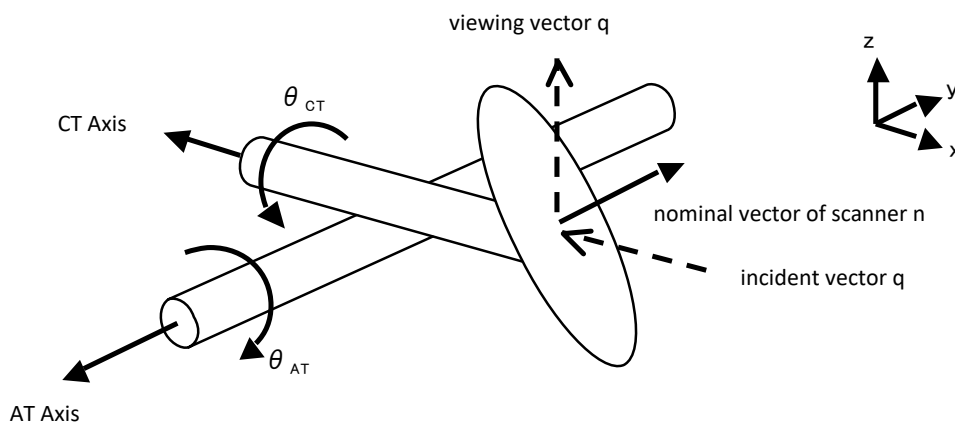


Fig. 2.3.7-2. Overview of scanner coordination

Eq. 2.3.7-1 defines normal vector of scanner n .

$$\begin{aligned} n &= \begin{pmatrix} \cos\theta_{AT} & 0 & \sin\theta_{AT} \\ 0 & 1 & 0 \\ -\sin\theta_{AT} & 0 & \cos\theta_{AT} \end{pmatrix} \begin{pmatrix} 1 & 0 & 0 \\ 0 & \cos\theta_{CT} & -\sin\theta_{CT} \\ 0 & \sin\theta_{CT} & \cos\theta_{CT} \end{pmatrix} \begin{pmatrix} \sin\left(\frac{\pi}{4}\right) \\ 0 \\ \sin\left(\frac{\pi}{4}\right) \end{pmatrix} \\ &= \frac{1}{\sqrt{2}} \begin{pmatrix} \cos\theta_{AT} + \sin\theta_{AT}\cos\theta_{CT} \\ -\sin\theta_{CT} \\ -\sin\theta_{AT} + \cos\theta_{AT}\cos\theta_{CT} \end{pmatrix} \end{aligned}$$

Eq. 2.3.7-1

Eq. 2.3.7-2 defines viewing vector q .

$$\begin{aligned}
q &= p - 2(p \cdot n)n = \begin{pmatrix} -1 \\ 0 \\ 0 \end{pmatrix} + (\cos\theta_{AT} + \sin\theta_{AT}\cos\theta_{CT}) \begin{pmatrix} \cos\theta_{AT} + \sin\theta_{AT}\cos\theta_{CT} \\ -\sin\theta_{CT} \\ -\sin\theta_{AT} + \cos\theta_{AT}\cos\theta_{CT} \end{pmatrix} \\
&= \begin{pmatrix} -1 + (\cos\theta_{AT} + \sin\theta_{AT}\cos\theta_{CT})^2 \\ -\sin\theta_{CT}(\cos\theta_{AT} + \sin\theta_{AT}\cos\theta_{CT}) \\ (\cos\theta_{AT} + \sin\theta_{AT}\cos\theta_{CT})(-\sin\theta_{AT} + \cos\theta_{AT}\cos\theta_{CT}) \end{pmatrix}
\end{aligned}$$

Eq. 2.3.7-2

Eq. 2.3.7-3 and Eq. 2.3.7-4 express the viewing vectors for AT (ϕ_{AT} : x-z plane angle) and CT (ϕ_{CT} : y-z plane angle), respectively.

$$\phi_{AT} = \text{atan} \left(\frac{-1 + (\cos\theta_{AT} + \sin\theta_{AT}\cos\theta_{CT})^2}{(\cos\theta_{AT} + \sin\theta_{AT}\cos\theta_{CT})(-\sin\theta_{AT} + \cos\theta_{AT}\cos\theta_{CT})} \right)$$

Eq. 2.3.7-3

$$\phi_{CT} = \text{atan} \left(\frac{-\sin\theta_{CT}}{(-\sin\theta_{AT} + \cos\theta_{AT}\cos\theta_{CT})} \right)$$

Eq. 2.3.7-4

2.4 TANSO-FTS-2 Acronyms

Acronym	Original description
FCE	Fringe Count Error
FFT	Fast Fourier Transformation
FTS	Fourier Transform Spectrometer
IGM	Interferogram
IMC	Image Motion Compensation
MOPD	Maximum Optical Path Difference
SPC	Spectra
ZPD	Zero Path Difference

2.5 TANSO-FTS-2 reference

Kuze, A., Suto, H., Nakajima, M., and Hamazaki, T.: Thermal and near infrared sensor for carbon observation Fourier-transform spectrometer on the Greenhouse Gases Observing Satellite for greenhouse gases monitoring, *Appl. Opt.*, 48, 6716–6733, 2009.

Keppel-Aleks, G., Toon, G. C., Wennberg, P. O., and Deutscher, N. M.: Reducing the impact of source brightness fluctuations on spectra obtained by Fourier-transform spectrometry, *Appl. Opt.*, 46, 4774–4779, 2007.

Kuze, A., Suto, H., Shiomi, K., Urabe, T., Nakajima, M., Yoshida, J., Kawashima, T., Yamamoto, Y., Kataoka, F., and Buijs, H.: Level 1 algorithms for TANSO on GOSAT: processing and on-orbit calibrations, *Atmos. Meas. Tech.*, 5, 2447–2467, doi:10.5194/amt-5-2447-2012, 2012.

Suto, H., Yoshida, J., Desbiens, R., Kawashima, T., Kuze, A.: Characterization and correction of spectral distortions induced by microvibrations onboard the GOSAT Fourier transform spectrometer, *Appl. Opt.*, 52, 4969–4980, 2013

R. O. Knuteson, H. E. Revercomb, F. A. Best, N. C. Ciganovich, R. G. Dedecker, T. P. Dirkx, S. C. Ellington, W. F. Feltz, R. K. Garcia, H. B. Howell, W. L. Smith, J. F. Short, and D. C. Tobin, “Atmospheric emitted radiance interferometer. Part I: Instrument design,” *J. Atmos. Ocean. Technol.*, vol. 21, no. 12, pp. 1763–1776, Dec. 2004.

R. O. Knuteson, H. E. Revercomb, F. A. Best, N. C. Ciganovich, R. G. Dedecker, T. P. Dirkx, S. C. Ellington, W. F. Feltz, R. K. Garcia, H. B. Howell, W. L. Smith, J. F. Short, and D. C. Tobin, “Atmospheric emitted radiance interferometer. Part II: Instrument performance,” *J. Atmos. Ocean. Technol.*, vol. 21, no. 12, pp. 1777–1789, Dec. 2004

H.E. Revercomb, H.Buijs, H.B.Howell, D.D.LaPorte, W.L.Smith and L.A. Sromovsky, “Radiometric calibration of IR Fourier transform spectrometers: solution to a problem with the High-Resolution Interferometer Sounder,” *Appl. Opt.*, 27, 3210-3218, 1988

NASA, Joint Polar Satellite System (JPSS) Cross Track Infrared Sounder (CrIS) Sensor Data Records (SDR) Algorithm theoretical Basis Document (ATBD), 2011

Suto, H., F. Kataoka, N. Kikuchi, R.O. Knuteson, A. Butz, M. Haun, H. Buijs, K. Shiomi, H. Imai, and A. Kuze (2020): Thermal and near-infrared sensor for carbon observation Fourier-transform spectrometer-2 (TANSO-FTS-2) on the Greenhouse Gases Observing Satellite-2 (GOSAT-2) during its first year on orbit. *Atmos. Meas. Tech. Discuss.*, <https://doi.org/10.5194/amt-2020-360>, in review.